JFM RAPIDS
journals.cambridge.org/rapids

Interrelation of phase-averaged volume force and capacitance of dielectric barrier discharge plasma actuators

M. Kuhnhenn[1,†], **B. Simon**[1], **I. Maden**[1] and **J. Kriegseis**[2]

[1]Institute for Fluid Mechanics and Aerodynamics, Technische Universität Darmstadt, Flughafenstraße 19, 64347 Griesheim, Germany

[2]Institute of Fluid Mechanics, Karlsruhe Institute of Technology (KIT), Kaiserstraße 10, 76131 Karlsruhe, Germany

Simultaneous measurements of the phase-averaged velocity distribution and the underlying discharge quantities of a dielectric barrier discharge plasma actuator (PA) are performed at 10 kHz discharge frequency to investigate the interplay of the discharge and the surrounding flow. The underlying velocity information for the force estimation is obtained by means of phase-averaged particle image velocimetry; the discharge quantities are determined from a Lissajous-figure analysis. The results uncover a clear cause–effect relation between the phase-dependent effective discharge capacitance of the PA and the resulting spatiotemporal volume-force distributions. From this novel insight, it must be concluded that the instantaneous effective discharge intensity dominates the momentum-transfer rate rather than the formerly assumed operating voltage.

Key words: flow control, MHD and electrohydrodynamics, plasmas

1. Background and objectives

The working principle of dielectric barrier discharge (DBD) plasma actuators (PAs) has been intensively investigated in the last decade, and was recently summarized by Benard & Moreau (2014), Kotsonis (2015) and Kriegseis, Simon & Grundmann (2016). Despite different overall perspectives, all three review publications emphasize the body-force distribution as being the main characteristic to understand and/or successfully predict the control mechanism of an operative PA and the effect of a discharge on a given flow scenario.

The variety of quasi-steady force-determination approaches has been contrasted by Kriegseis *et al.* (2013). More recently, Debien *et al.* (2012) and Neumann *et al.*

(2013), for instance, successfully determined the phase-averaged force magnitude of a PA by means of particle image velocimetry (PIV) and laser Doppler velocimetry respectively. Moreover, based on the Navier–Stokes approach suggested by Wilke (2009), the desired spatiotemporal force distribution of a PA was recently provided by Benard, Debien & Moreau (2013).

Although there are several publications about the development of the volume force, there is no obvious agreement about the exact behaviour. It is widely accepted that the AC character of the operating voltage and thus the plasma discharge leads to different contributions to the force in the positive and negative half-cycles, as shown by Enloe, McHarg & McLaughlin (2008) and Orlov, Font & Edelstein (2008). Most of the abovementioned investigations used a sinusoidal high-voltage signal with a frequency in the range of 1 kHz to identify the phase relation of the measured volume force. Since the operating voltage was used to indicate the electric/fluid mechanical interrelation, only indirect phase information on the cause–effect relation between the discharge and the resulting force distributions was provided.

At higher operation frequencies of approximately 10 kHz, lightweight high-voltage transformers can be used, allowing in-flight studies as demonstrated by Duchmann *et al.* (2014). The investigations by Neumann *et al.* (2013) were performed at 9.5 kHz and provide the first valuable information on the phase-averaged force magnitude in this range of frequencies. However, even though promising for flight applications, to date, no investigation into the spatiotemporal force distribution has been published for such high frequencies.

The purpose of the present work, therefore, is twofold. First, phase-resolved PIV measurements are conducted at an operation frequency of $f = 10$ kHz to provide phase-averaged velocity and force information for such fast discharge cycles. Here, the involved competition between an appropriate particle displacement and a reasonable phase resolution pushes this measurement technique to its limits. Additionally, together with the simultaneously measured discharge cyclograms (Lissajous figures), the hypothesis is tested of whether or not the temporal evolution of the discharge capacitance C_{eff} (and thus the discharge intensity) is in phase with the resulting force magnitude and possibly its corresponding distribution.

2. Actuator working principle and Lissajous-figure analysis

A sketch of a DBD PA in surface discharge mode is shown in figure 1(*a*). Typically, the actuator consists of an upper (exposed) electrode, a dielectric and a lower (covered) electrode. The dielectric used in this experiment is made of Kapton® ($d = 0.4$ mm polyimide) with high permittivity. The two copper electrodes are arranged with no overlap or gap, such that the horizontal distance between b_1 and b_2 is zero. An AC voltage with a magnitude of several kilovolts is applied to the upper electrode and the lower electrode is grounded.

The resulting electric field periodically exceeds the breakdown field strength E_b, such that air ionizes and plasma discharge occurs in both half-cycles. Accelerated by the electric field, the ions collide with the surrounding neutrals and thus impart momentum to the gas, which is commonly referred to as body or volume force. Like in the present study, experimental investigations into this force have mostly been performed in quiescent air, where the momentum transfer results in a wall jet of several metres per second magnitude.

During either half-cycle, the plasma layer gradually grows along the dielectric surface right after discharge onset ($E \geqslant E_b$) and eventually collapses at the highest
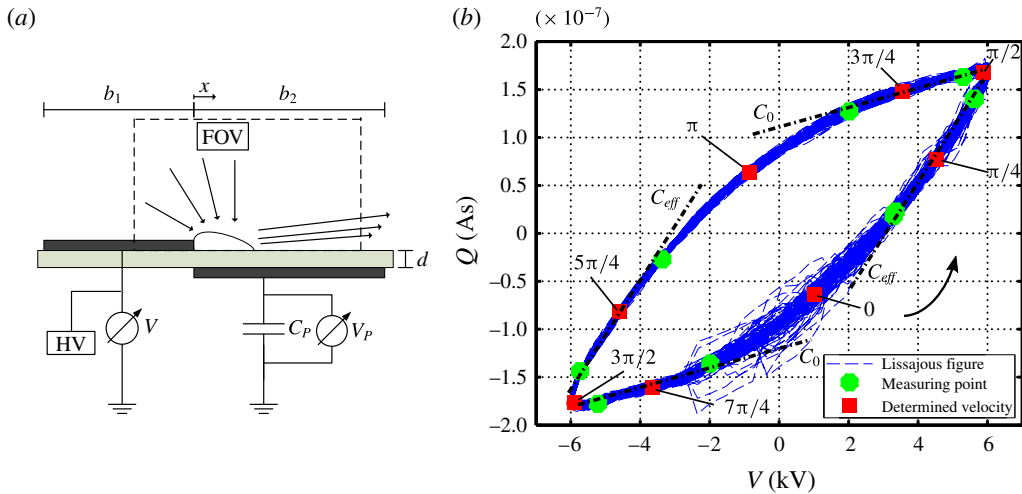
FIGURE 1. (*a*) Set-up of a DBD PA with two electrodes b_1, b_2 and a dielectric with a thickness of d. The field of view (FOV) is shown for clarity (dashed box). In addition, the electric measurement equipment is indicated. (*b*) Charge $Q = C_P V_P$ and operating voltage V of the same DBD actuator plotted in a Lissajous figure (Q–V cyclogram) with characteristic capacitances C_0 and C_{eff} (dashed lines). Furthermore, the acquisition points for the PIV measurements and the effective phases of the respectively determined velocity fields are emphasized.

intensity right at the positive, respectively negative, peak voltage. However, even though similar at first glance, the discharges of the half-cycles show distinct differences, which were elaborated in detail, e.g., by Gibalov & Pietsch (2000). A streamer-like discharge comprising multiple distinct current peaks occurs during the positive half-cycle, whereas a more uniform glow discharge is maintained during the negative half-cycle. It should be noted that, similarly to the half-cycle distinction, the terms forward and backward stroke are also frequently used; see, e.g., Enloe *et al.* (2008).

The instantaneous discharge properties, i.e. operating voltage $V(t)$ and released charge $Q(t) = C_P V_P(t)$, can be easily recorded by means of a high-voltage probe and across an appropriate probe capacitor respectively, which are also sketched in figure 1(*a*). If plotted against each other, the resulting Lissajous figure (discharge cyclogram) provides information on the consumed actuator power P_A. Moreover, the instantaneous or phase-averaged discharge capacitance can be determined from the slope of the cyclogram according to

$$C(t) = \frac{dQ(t)}{dV(t)} \quad \text{or} \quad C(\phi) = \frac{\Delta Q(\phi)}{\Delta V(\phi)} \quad (2.1a,b)$$

respectively. Figure 1(*b*) shows the Lissajous figure for the investigated actuator, where two characteristic capacitances are indicated. The capacitance C_0 describes the pure passive (cold) capacitance of the PA, which occurs during the so-called dark periods (Manley 1943), when no discharge is present. The effective discharge capacitance C_{eff} consists of a combination of C_0 and the capacitance of the plasma itself, and thus reveals a steeper slope in the cyclogram than C_0. One should refer to Kriegseis *et al.* (2011) for more details on the analysis of PA-specific discharge cyclograms.

809 R1-3

3. Experimental procedure and PIV processing

The required velocity information for the force-determination approach is recorded with a 2D–2C PIV set-up comprising a dual-cavity Nd:YLF laser (Litron LDY303-PIV), a high-speed camera (Phantom V12, 800×600 pixel resolution) and a reversely mounted Schneider-Kreuznach SKR SYMMAR 120/5.6 lens. The FOV spans 9 mm $\times$ 6.7 mm in the immediate vicinity above the actuator (see figure 1a), resulting in a resolution of approximately 88 pixel mm^{-1}. To ensure a quiescent environment for the wall-jet measurements, the experiments are conduced in a plexiglass containment, which is seeded with di-ethyl-hexyl-sebacat (DEHS) tracers with a mean diameter of $d_p = 0.9$ µm. The corresponding particle response time of the tracers is determined as $\tau_p = \rho_p d_p^2 / 18\eta = 2.25$ µs, with ρ_p and η for the DEHS density and dynamic viscosity of air respectively (see, e.g., Raffel *et al.* 2007).

The actuator is operated with a GBS Minipuls 6 at a frequency of $f = 10$ kHz and $V_{pp} = 12$ kV (sine), which implies maximum horizontal jet velocities in the range of $u = 7$ m s^{-1} for this actuator (see Kriegseis *et al.* 2013). Accordingly, the Stokes number of the problem is determined as $Stk = \tau_p u / l_c = 1.6 \times 10^{-2}$, where $l_c = 1$ mm is the characteristic length scale of the problem (see, e.g., Durscher & Roy 2012). The operating voltage V and charge probe voltage V_p are acquired with a USB oscilloscope (Pico-Scope 4424, sample rate 1 MS s^{-1}) and directly processed with LabVIEW. Eight different phases per discharge cycle are recorded for the velocity information, which, in contrast to previous studies, are precisely adjusted to the capacitance information of the Lissajous figure; see figure 1(b). Each half-cycle is subdivided into four consecutive phases to particularly provide information during (i) the dark period at C_0, (ii) the discharge onset/transition, (iii) the effective discharge at C_{eff} and (iv) the corners of the cyclogram, where the discharge ceases.

The camera and laser are triggered and synchronized with a digital timer card (LabVIEW, NI PCI-6602), which also serves as a time base for the PA operation frequency. The PIV set-up is operated in double-frame mode at a repetition rate of $f_{cam} = 3200$ Hz, since the base clock of the NI timer card ($f_{NI} = 80$ MHz) only supports discrete recording frequencies with a common factor. The laser pulse distance is accordingly set to $\Delta t = 12.5$ µs between frames, which results in a maximum particle displacement of $\Delta x_{max} \approx 7$ pixel for the expected velocities. As such, it is furthermore possible to record the eight phase angles in a permutating way in only one measurement. For the given memory (8 GB) of the camera, 10 000 frames can be captured, resulting in 625 image pairs per phase angle. The phase angle of the first frame of the measurements is identified retroactively from the camera trigger and the Q-switch signal of laser cavity 1 in comparison with the discharge signals.

All image pairs are processed with commercial software (PIVTEC, PIVview), where a multigrid cross-correlation algorithm with an initial/final interrogation area (IA) size of $64 \times 64/8 \times 8$ pixel is applied. To ensure statistical significance of the obtained data, a convergence study is conducted. Figure 2 shows the relative standard deviation of the velocity, $\sigma^* = \sigma_u / \bar{u}$ (averaged over 3×3 IA), as a function of an increasing number of image pairs, where the considered images are equally distributed over the complete range of available images (per phase angle). Figure 2(a) compares the convergence properties for different characteristic locations in the wall jet. Complementarily, the convergence behaviour for all phases is additionally tested in figure 2(b) for the fully developed wall jet.

Both diagrams saliently demonstrate that an order of magnitude of 10^2 image pairs is sufficient to ensure statistical significance of the data. The main reason for this
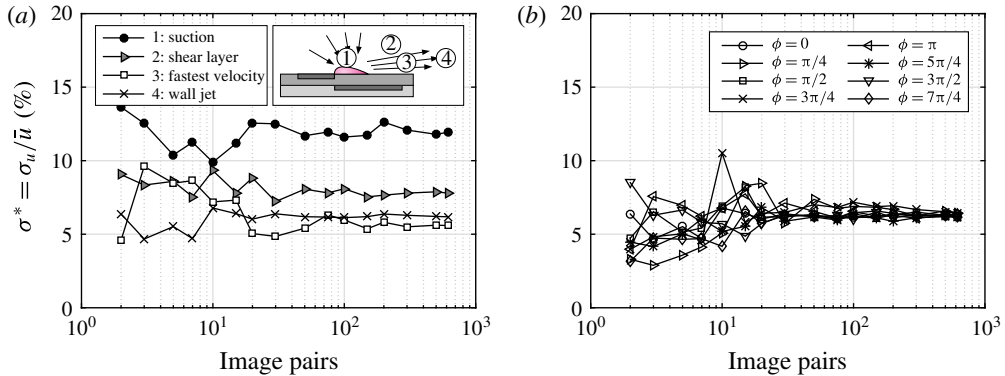
FIGURE 2. Statistical significance of the PIV data: convergence of the relative standard deviation $\sigma^* = \sigma_u/\bar{u}$ for (*a*) four characteristic locations of the wall jet at $\phi = 0$ and (*b*) the fully developed wall jet ④ for all phase angles as indicated in figure 1(*b*).

comparatively fast convergence is that the measurements are conducted at distinct phase angles in the cycle. The velocities of the wall jet only differ slightly if the same phase angle and therefore the same working point of the PA is used for the correlation of the image pairs. This technique makes it possible to use a small number of image pairs for the correlation – in contrast to time-averaged investigations without paying attention to the operation point in the cycle (at least an order of magnitude of 10^3 image pairs in, e.g., Benard & Moreau (2011) and Kriegseis *et al.* (2013)). Furthermore, the measurements are repeated three times to ensure reproducibility of the experimental results.

4. Volume-force determination

The generated horizontal volume force $f_i(x_j, t)$ is determined using the two-dimensional Navier–Stokes equation (NSE) of a Newtonian incompressible fluid ($D\rho/Dt = 0$) with constant dynamic viscosity η,

$$f_i = \underbrace{\rho \frac{\partial u_i}{\partial t}}_{\text{local acceleration}} + \underbrace{\rho u_j \frac{\partial u_i}{\partial x_j}}_{\text{convective acceleration}} - \underbrace{\eta \frac{\partial^2 u_i}{\partial x_j \partial x_j}}_{\text{diffusion}}, \qquad (4.1)$$

where, furthermore, the pressure gradient is neglected as proposed (and retroactively verified) by Wilke (2009). It should be noted that only f_x is considered in the present study, since earlier studies demonstrated that the horizontal force f_x is predominant in the problem by orders of magnitude, i.e $f_x \gg f_y$ (e.g. Benard *et al.* 2013). Further evidence for the validity of the above assumptions was provided by Dörr & Kloker (2015) based on direct numerical simulations (DNS). In their comprehensive investigation into various influential factors on the accuracy of the resulting force estimation, the above simplifications were further confirmed to be appropriate for the horizontal component in quiescent air.

The right-hand side of (4.1) comprises acceleration, convection and diffusion terms. The latter two terms can be calculated straightforwardly from the respective phase information $u_i(x, y, \phi)$. The phase-to-phase deviations of the first term are
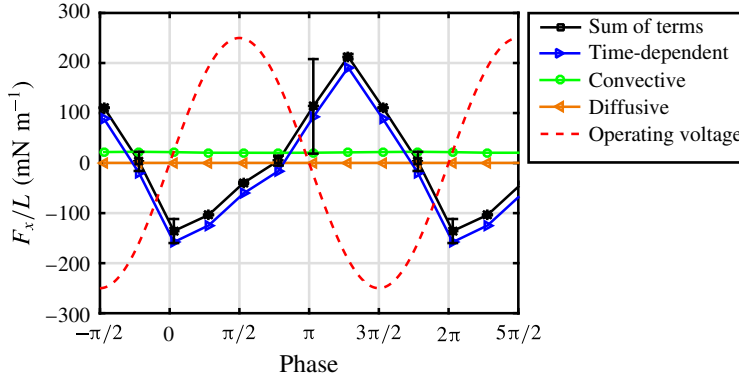
809 R1-5

FIGURE 3. Decomposition of the volume force F_x into convective, diffusive and time-dependent parts. The error bars indicate the reproducibility based on three measurements for the overall volume force.

approximated via central differences according to

$$\frac{\partial u(x, y, t)}{\partial t} \approx \frac{u(x, y, \phi + \Delta\phi) - u(x, y, \phi - \Delta\phi)}{t(\phi + \Delta\phi) - t(\phi - \Delta\phi)}. \tag{4.2}$$

It is worth mentioning that the accuracy of the acceleration term (4.2) immediately depends on the number of distinguished phases, where the latter is limited by sufficient minimum particle displacement (cf. §3). In order to directly compare the impacts of the contributions of (4.1), the force distribution f_x is integrated across the control volume (CV),

$$\frac{F_x(\phi)}{L} = \iint_{CV} f_x(x, y, \phi) \, \mathrm{d}A, \tag{4.3}$$

and compared with all separate terms, all of which are similarly integrated across the CV. The comparison is plotted in figure 3. Obviously, the periodic contribution of local acceleration is most dominant in the diagram. The convective term is an order of magnitude weaker at almost constant values in the range of 20 mN m^{-1} across all phase angles. In contrast, the contribution of the acceleration term centres around zero and therefore vanishes for a time-averaged approach.

Scatter and/or limited reproducibility of the data is indicated as error bars in figure 3, which only reveals noticeable uncertainties for the discharge onset at $\phi = 0$ and $\phi = \pi$. Here, in particular, the scattered discharge of the filamentary streamer discharge of the positive half-cycle at $\phi = 0$ and the variable discharge onset of the glow discharge in the negative half-cycle at $\phi = \pi$ result in considerable variance (cf. figure 1b). This in turn leads to a small change of the velocity gradient $\partial u/\partial t$, causing the change in the resulting volume force.

The spatial distribution of all NSE terms is shown in figure 4 for $\phi = \pi$ to illustrate the respective contributions to the overall force distribution. As above, the local acceleration $\rho \, \partial u/\partial t$ is predominant over the convective acceleration $\rho u \, \partial u/\partial x$ throughout the field. A closer look at the latter still reveals a positive volume force with horizontal direction in the left part of the FOV; see figure 4(b). This is due to the positive gradient $\partial u/\partial x$ in this part of the wall jet. The overall contribution of the diffusive (viscous) term is almost negligible: only a thin layer immediately above
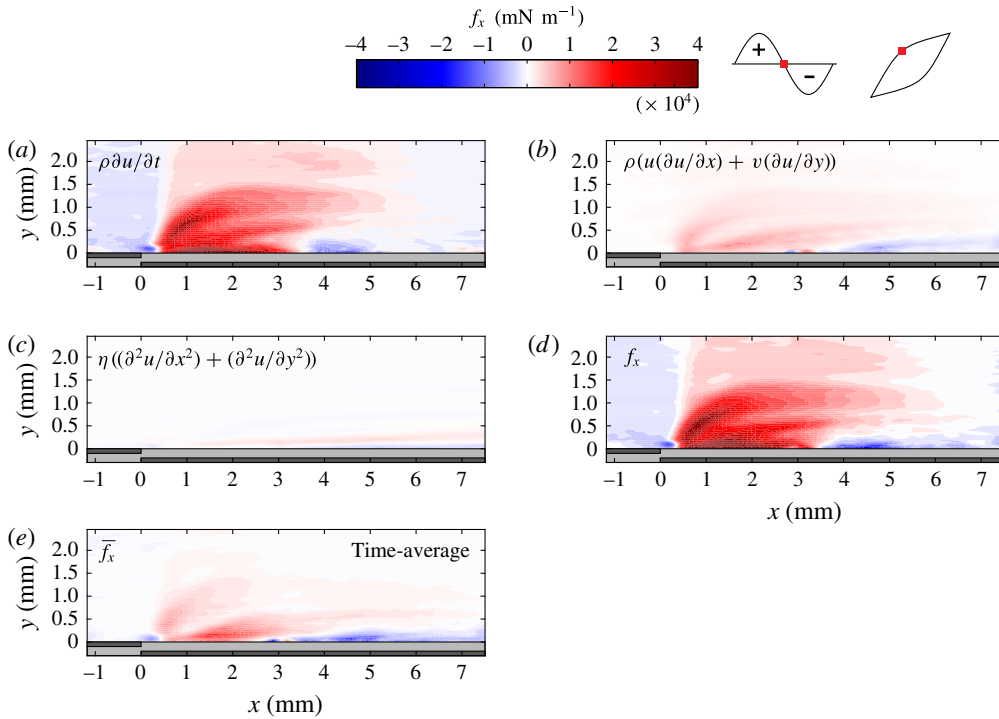
FIGURE 4. Contribution of all NSE terms to the force distribution (phase angle $\phi = \pi$ is shown): (*a*) local acceleration $\rho \, \partial u / \partial t$, (*b*) convective terms $\rho u_j \, \partial u_i / \partial x_j$, (*c*) diffusive terms $\eta \, \partial^2 u_i / \partial x_j \partial x_j$, (*d*) overall volume force f_x as the sum of all terms (*a–c*) according to equation (4.1). (*e*) The time-averaged volume force $\overline{f_x}$ is added for comparison purposes.

the dielectric has a rather mild impact on the local force distribution (cf. figures 3 and 4*c*). Furthermore, the influence of shearing forces in the boundary layer further downstream results in a negative contribution to the volume force (Kriegseis *et al.* 2013). As outlined above, the time-averaged force distribution is mostly dominated by the quasi-steady convective term (cf. figures 4*b,e*).

5. Interrelation of capacitance and volume force

Figure 3 already indicated a mostly negative volume force F_x in the positive half-cycle, which then ceases right after the voltage slope changes sign at $\phi = \pi/2$. Similarly, the negative half-cycle yields largely positive forces until the voltage slope changes sign again at $\phi = 3\pi/2$. Comparison of the force histories with figure 1(*b*) reveals that this force breakdown coincides with collapse of the discharge in either corner of the cyclogram, where the effective discharge capacitance C_{eff} falls back to the cold capacitance C_0. In addition, figure 5 provides the volume-force distribution $f_x(x, y, \phi)$ for all eight examined phase angles, where the positive and negative half-cycles appear in (*a,c,e,g*) and (*b,d,f,h*) respectively. The evaluated phase angles for either half-cycle are indicated at the top of the figure.

Starting from the cold capacitance $\phi = 7\pi/4$, the positive half-cycle begins at $\phi = 0$ with the onset of the filamentary streamer discharge, which immediately leads to the maximum negative volume force. Due to the filamentary character of the plasma,
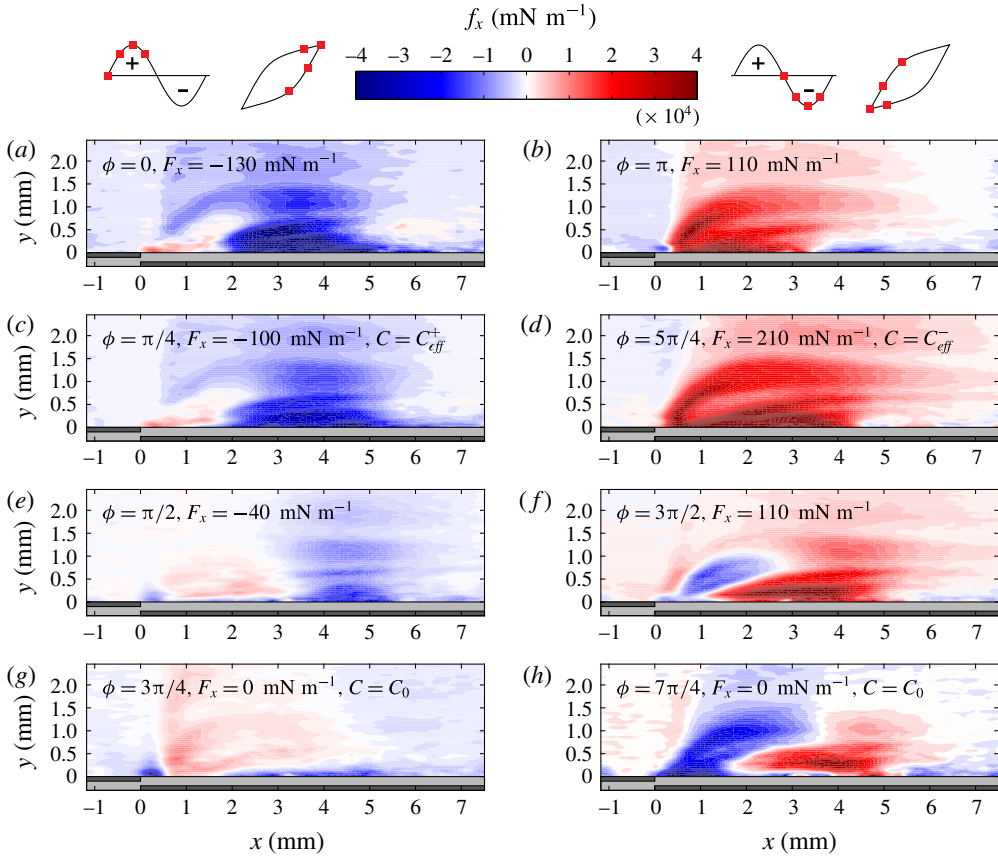
FIGURE 5. Volume-force distribution $f_x(x, y, \phi)$ for all evaluated phase angles ϕ. The positive and negative half-cycles appear in (a,c,e,g) and (b,d,f,h) respectively, as denoted at the top of the figure; (a,b), (c,d), (e,f) and (g,h) accordingly provide the force fields during discharge onset/transition, effective discharge intensity with C_{eff}, collapse of the plasma and dark period with C_0 respectively.

in particular the area in the range 2 mm $< x <$ 5 mm massively contributes to the force (cf. also Gibalov & Pietsch 2000). This force distribution is maintained at a slightly lower force level for the duration of the streamer discharge, which develops the effective discharge intensity C_{eff}^+ at $\phi = \pi/4$, which then collapses once the peak voltage is crossed at $\phi = \pi/2$ (see also the upper right corner of the cyclogram in figure 1b). Accordingly, the negative force domain fades away and is compensated by traces of positive force contributions, which finally cancel each other out once the discharge entirely drops during the dark period. As such, the actuator force is zero during the cold capacitance C_0 at $\phi = 3\pi/4$.

The more uniform glow discharge of the negative cycle starts at $\phi = \pi$, where, in contrast to the streamer discharge, the positive force starts to develop immediately next to the exposed electrode and covers the area in the range 0 mm $< x <$ 3 mm at comparable magnitude to the positive half-cycle ($\phi = \pi$). During this diffusive discharge, the electrons, and more importantly the negative oxygen ions (see Boeuf, Lagmich & Pitchford 2009), move from the upper exposed electrode onto the surface of the dielectric. Accordingly, both the force domain and magnitude continuously
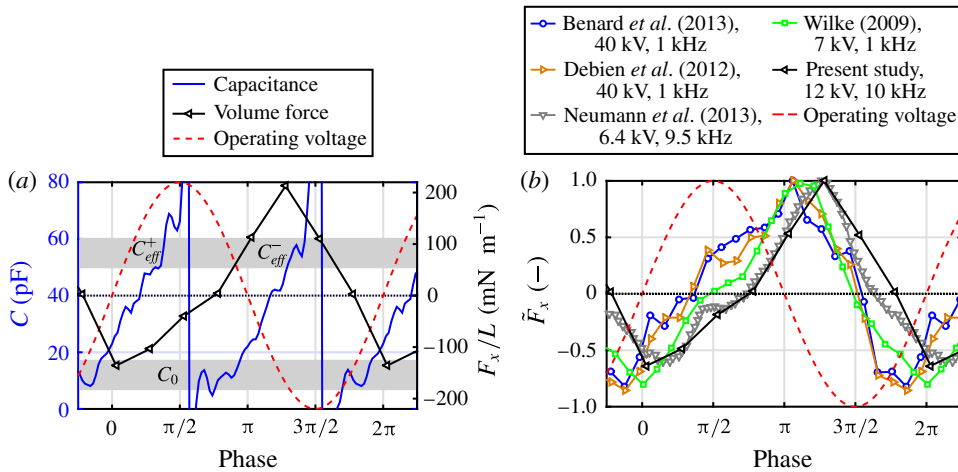
FIGURE 6. Phase-averaged actuator volume force: (*a*) interrelation of the phase-averaged capacitance C and the volume force F_x; note that the left ordinate starts from zero, whereas the right ordinate centres around zero; (*b*) comparison of normalized magnitudes $\tilde{F}_x(\phi) = F_x(\phi)/\max|F_x(\phi)|$ with the literature.

grow towards C_{eff}^- at $\phi = 5\pi/4$. Like with the positive peak voltage ($\phi = \pi/2$), the discharge similarly ceases at the negative peak voltage at $\phi = 3\pi/2$, where the plasma collapses again. Accordingly, the competition of positive and negative force contributions begins and the force magnitude drops. Finally, even though at higher magnitudes compared with $\phi = 3\pi/4$, again the positive and negative parts of the force field happen to perfectly cancel each other out during the cold capacitance C_0 at $\phi = 7\pi/4$.

To emphasize the interrelation of the actuator capacitance C and the resulting force F_x/L more saliently, both quantities are plotted atop the phase angle ϕ in figure 6(*a*). It should be noted that the capacitance has been averaged cycle-wise in the diagram and the occurrence of the characteristic capacitances, C_0 and C_{eff}, is highlighted grey in the diagram.

Most remarkably, there is no volume force F_x during the dark periods with the cold capacitance C_0 at the two phase angles $\phi = 3\pi/4$ and $\phi = 7\pi/4$. Furthermore, in accordance with the investigations of Kriegseis *et al.* (2011), the effective discharge capacities C_{eff}^- and C_{eff}^+ are very similar in both half-cycles. However, it has already been demonstrated in figure 5 that the different discharge regimes nonetheless lead to significant deviations of both the force distribution $f_x(x, y, \phi)$ and the force magnitude $F_x(\phi)$. The resulting difference in magnitude becomes especially obvious from direct comparison of the two half-cycles in figure 5.

Additionally, the difference in relative phase angle (per half-cycle) for the force peak demonstrates the influence of the gradual plasma growth of the glow in contrast to the fast development of the streamer discharge on the resulting force production. From the given phase resolution of the present data, a phase-angle shift of approximately $\Delta_\phi^\pm \approx \pi/4$ is estimated. In particular, the positive force peak of the negative half-cycle is found to perfectly coincide with the effective discharge capacitance C_{eff}^- at $\phi = 5\pi/4$, whereas the negative peak already occurs at $\phi = 0$ (thus before a fully developed C_{eff}^+) at approximately 50 % in strength.

The phase-averaged force magnitudes $F_x(\phi)$ are furthermore compared with the literature in figure 6(*b*), where the results of equation (4.3) appear normalized according to $\tilde{F}_x(\phi) = F_x(\phi)/\max|F_x(\phi)|$ to account for the different geometry configurations and operating conditions of the respective PAs.

It is obvious from first glance that all studies reveal negative and positive contributions to the actuator force during the positive and negative half-cycles respectively. Moreover, the aforementioned phase-angle shift between the two half-cycles can be recognized in all of the curves of the diagram, which provides evidence for the physical significance of this shift. Interestingly, an additional (constant) phase lag of approximately $\pi/4$ between the studies in the ranges of 1 kHz (Wilke 2009; Debien *et al.* 2012; Benard *et al.* 2013) and 10 kHz (Neumann *et al.* 2013, present study) can be identified. On a technical note, the particle relaxation time of the DEHS tracers, $\tau_p = 2.25 \ \mu s$, implies phase lags of $\Delta_\phi^{\tau_p} \approx \pi/200$ and $\Delta_\phi^{\tau_p} \approx \pi/20$ for PA operation at 1 kHz and 10 kHz respectively, which in either case is well below the observed phase lag. It is, therefore, hypothesized that the momentum transfer from the plasma to the surrounding air also comprises a certain (frequency-dependent) response time.

6. Concluding remarks

In agreement with the literature, the present results show that a positive volume force $F_x > 0$ is generated by a DBD PA in the negative half-cycle during the glow discharge and a negative volume force $F_x < 0$ is formed in the positive half-cycle during the streamer discharge. The new approach of using arbitrary phase angles across the cycle can help to drastically reduce the number of data sets needed for statistical significance. The phase-averaged force distributions $f_x(x, y, \phi)$ provide valuable insight into the origin of the observed phase-angle shift $\Delta_\phi^\pm$ of the force peaks between the two half-cycles. In particular, this shift is concluded to rely on the different discharge scenarios (streamer and glow). The additional phase lag of the PA force production when operated at higher frequencies is demonstrated to not result from the finite particle response time τ_p of the chosen tracers. Consequently, it is hypothesized that the plasma-to-air momentum transfer itself involves a (frequency-dependent) delay. A detailed analysis of this hypothesis is obviously beyond the scope of the present work and is foreseen to be addressed in future investigations.

Simultaneous consideration of the corresponding discharge cyclograms (Lissajous figures) uncovers the dependence of the generated volume force on the instantaneous capacitance $C(t)$ of the PA rather than the underlying operating voltage $V(t)$. This phase distinction according to the instantaneous discharge situation provides clear formerly hidden cause–effect relations, where even the footprint of the higher discharge scatter level during discharge onset can be immediately identified in the uncertainty margin of the resulting force magnitudes. The main part of the plasma discharge at C_{eff} shows the major contribution to the resulting volume force. Importantly, during dark periods, and thus passive capacitance C_0, the overall volume force is counterbalanced to approximately zero. The periodic formation of the volume-force distribution and moreover the corresponding interrelation of the discharge and the resulting momentum transfer, as identified in the present study, can help in the design of novel and innovative control concepts in discharge-based closed-loop control applications in aerodynamics. Additionally, this new insight might serve as a basis for advanced model development of the PA source term for numerical simulations.

References

BENARD, N., DEBIEN, A. & MOREAU, E. 2013 Time-dependent volume force produced by a non-thermal plasma actuator from experimental velocity field. *J. Phys. D: Appl. Phys.* **46**, 245201.

BENARD, N. & MOREAU, E. 2011 On the vortex dynamic of airflow reattachment forced by a single non-thermal plasma discharge actuator. *Flow Turbul. Combust.* **87** (1), 1–31.

BENARD, N. & MOREAU, E. 2014 Electrical and mechanical characteristics of surface ac dielectric barrier discharge plasma actuators applied to airflow control. *Exp. Fluids* **55** (11), 1846.

BOEUF, J. P., LAGMICH, Y. & PITCHFORD, L. C. 2009 Contribution of positive and negative ions to the electrohydrodynamic force in a dielectric barrier discharge plasma actuator operating in air. *J. Appl. Phys.* **106** (2), 023115.

DEBIEN, A., BENARD, N., DAVID, L. & MOREAU, E. 2012 Unsteady aspect of the electrohydrodynamic force produced by surface dielectric barrier discharge actuators. *Appl. Phys. Lett.* **100**, 013901.

DÖRR, P. C. & KLOKER, M. J. 2015 Numerical investigation of plasma-actuator force-term estimations from flow experiments. *J. Phys. D: Appl. Phys.* **48** (39), 395203.

DUCHMANN, A., SIMON, B., TROPEA, C. & GRUNDMANN, S. 2014 Dielectric barrier discharge plasma actuators for in-flight transition delay. *AIAA J.* **52** (2), 358–367.

DURSCHER, R. & ROY, S. 2012 Evaluation of thrust measurement techniques for dielectric barrier discharge actuators. *Exp. Fluids* **53** (4), 1165–1176.

ENLOE, C. L., MCHARG, M. G. & MCLAUGHLIN, T. E. 2008 Time-correlated force production measurements of the dielectric barrier discharge plasma aerodynamic actuator. *J. Appl. Phys.* **103**, 073302.

GIBALOV, V. I. & PIETSCH, G. J. 2000 The development of dielectric barrier discharges in gas gaps and on surfaces. *J. Phys. D: Appl. Phys.* **33** (20), 2618.

KOTSONIS, M. 2015 Diagnostics for characterisation of plasma actuators. *Meas. Sci. Technol.* **26** (9), 092001.

KRIEGSEIS, J., MÖLLER, B., GRUNDMANN, S. & TROPEA, C. 2011 Capacitance and power consumption quantification of dielectric barrier discharge (dbd) plasma actuators. *J. Electrostat.* **69**, 302–312.

KRIEGSEIS, J., SCHWARZ, C., TROPEA, C. & GRUNDMANN, S. 2013 Velocity-information-based force-term estimation of dielectric-barrier discharge plasma actuators. *J. Phys. D: Appl. Phys.* **46**, 055202.

KRIEGSEIS, J., SIMON, B. & GRUNDMANN, S. 2016 Towards in-flight applications? A review on dielectric barrier discharge-based boundary-layer control. *Appl. Mech. Rev.* **68** (2), 020802.

MANLEY, T. C. 1943 The electric characteristics of the ozonator discharge. *J. Electrochem. Soc.* **84** (1), 83–96.

NEUMANN, M., FRIEDRICH, C., CZARSKE, J., KRIEGSEIS, J. & GRUNDMANN, S. 2013 Determination of the phase-resolved body force produced by a dielectric barrier discharge plasma actuator. *J. Phys. D: Appl. Phys.* **46**, 042001.

ORLOV, D. M., FONT, G. I. & EDELSTEIN, D. 2008 Characterization of discharge modes of plasma actuators. *AIAA J.* **46** (12), 3142–3148.

RAFFEL, M., WILLERT, C., WERELEY, S. & KOMPENHANS, J. 2007 *Particle Image Velocimetry: A Practical Guide*. Springer.

WILKE, J. B. 2009 Aerodynamische Strömungssteuerung mittels dielektrischen Barriereentladungs-Plasmaaktuatoren. PhD thesis, DLR Göttingen, Germany.